*The Origin of Outflows in Evolved Stars*
*Proceedings IAU Symposium No. 366, 2022*
*L. Decin, A. Zijlstra & C. Gielen, eds.*
doi:10.1017/S1743921322000230

# The first 3D models of evolved hot star outflows

**Nicolas Moens and Levin Hennicker**

Instituut voor Sterrenkunde, KU Leuven, Celestijnenlaan 200D, 3001 Leuven, Belgium
email: nicolas.moens@kuleuven.be

**Abstract.** The mechanisms driving mass loss from massive stars in late stages of their evolution is still very much unknown. Stellar evolution models indicate that the last stage before going supernova for many massive stars is the Wolf-Rayet (WR) phase, characterized by a strong, optically thick stellar wind. Stellar models show that these stars exceed the Eddington limit already in deep sub-surface layers around the so-called 'iron-opacity' bump, and so should launch a supersonic outflow from there. However, if the outward force does not suffice to accelerate the gas above the local escape speed, the initiated flow will stagnate and start raining down upon the stellar core. In previous, spherically symmetric, WR wind models, this has been circumvented by artificially increasing either clumping or the line force. Here, we present pioneering 3D time-dependent radiation-hydrodynamic simulations of WR winds. In these models, computed without any ad-hoc force enhancement, the stagnated flow leads to co-existing regions of up- and down-flows, which dynamically interact with each other to form a multi-dimensional and complex outflow. These density structures, and the resulting highly non-monotonic velocity field, can have important consequences for mass-loss rates and the interpretation of observed Wolf-Rayet spectra.

**Keywords.** Stars: Wolf-Rayet, Radiation: dynamics, Methods: numerical, Hydrodynamics

## 1. Introduction

The Wolf-Rayet (WR) phase is thought to be the last phase in the lives of many stars that are born with an initial mass higher than $\sim 25\,M_\odot$ (Crowther 2007). These stars play an essential role in the chemistry and gas dynamics of their host galaxies, not only because of their strong stellar wind, but also because mass loss in the WR phase determines the type of compact object left after a supernova explosion. WR stars are hot, evolved, compact stars that are observationally characterised by strong, broad emission lines in the optical spectrum. This emission originates in the strong, optically thick stellar wind that surrounds the star.

WR stars have typical masses between $10\,M_\odot$ and $25\,M_\odot$ (Crowther 2007). Their winds have high terminal speeds and high mass-loss rates on the order of $10^{-7} - 10^{-4}\,M_\odot\,\mathrm{yr}^{-1}$ (Hamann *et al.* 2019; Nugis & Lamers 2000). Despite the importance of this final evolutionary phase, the wind launching mechanism is not yet completely understood. Recent theoretical work has put forward a mechanism that combines the effects of line driving with the enhanced radiation force over the Rosseland mean opacity bump due to iron recombination to successfully model the winds of WR stars in a spherically symmetric, 1D setup (Poniatowski et al. 2021).

However, due to convective instabilities in the high Eddington ratio environment close to the star's hydrostatic core, the wind is believed to be prone to structure formation, breaking its spherical symmetry. It is expected that due to this structure formation,

the wind of a WR star might be very turbulent. Perhaps not all material that is initially lifted from the stellar surface will be able to completely reach escape velocity before falling back down. Wind inhomogeneities such as described here are believed to be the cause of line profile variations (LPV's) that have been observed for WR stars (Lépine & Moffat 1999).

To understand these effects, WR winds need to be modelled in a time-dependent, multi-dimensional framework, where the radiation force is accurately taken into account by including both the effects of line driving and the iron opacity peak. Here we describe the technique and present the first models that simulate such 3D time-dependent structure formation.

## 2. Methodology

### 2.1. *Equations of radiation hydrodynamics*

We present models that are obtained by solving the radiation-hydrodynamics (RHD) equations on a 2D and 3D finite volume mesh in a pseudo-planar, box-in-a-wind approach (see, e.g., Sundqvist et al. 2018). Our numerical domain starts at the hydrostatic core of the star $R_{\rm core}$, is 5 $R_{\rm core}$ long in the radial direction and has a width of 0.5 $R_{\rm core}$ in (both) lateral directions. Gravity is assumed to originate from a point source and we take into account the cooling, heating, and forces due to radiation. The exact equations solved are the conservative equations of hydrodynamics together with the frequency integrated, zeroth moment of the radiative transfer equation (RTE) (see also Moens et al. 2021):

$$\partial_t \rho + \nabla \cdot (\rho \mathbf{v}) = 0, \tag{2.1}$$

$$\partial_t (\mathbf{v}\rho) + \nabla \cdot (\mathbf{v}\rho\mathbf{v} + p) = -\rho \frac{GM}{r^2}\hat{r} + \rho\frac{\kappa \mathbf{F}}{c}, \tag{2.2}$$

$$\partial_t e + \nabla \cdot (e\mathbf{v} + p\mathbf{v}) = -\mathbf{v} \cdot \rho \frac{GM}{r^2}\hat{r} + \mathbf{v} \cdot \rho\frac{\kappa \mathbf{F}}{c} + c\kappa\rho E - 4\pi\kappa\rho B(T_g), \tag{2.3}$$

$$\partial_t E + \nabla \cdot (E\mathbf{v} + \mathbf{F}) = -\nabla\mathbf{v} : P - c\kappa\rho E + 4\pi\kappa\rho B(T_g). \tag{2.4}$$

In the equations above, $\rho$, $\mathbf{v}$, $e$, and $p$ are the hydrodynamic gas density, gas velocity, gas total energy density and gas pressure. $E$, $\mathbf{F}$ and $P$ are the frequency integrated radiation energy density, radiation flux, and radiation pressure. $G$ and $M$ are Newton's gravitational constant and the mass of the stellar object. $B(T_g)$ is the frequency integrated Planck function of a gas with temperature $T_g$. Finally, $\kappa$ is the frequency integrated mass absorption coefficient or opacity. This is the interaction constant between the gas and radiation variables and is a crucial quantity in our models. We here assume that $\kappa$ is isotropic and that the flux mean, Planck mean and energy mean opacities are all equal. On the right hand side of Eq. (2.2), source terms are included that correspond to gravity and the force due to radiation. In Eqs (2.3)–(2.4), source terms include heating and cooling of the gas due to radiation, as well as the terms corresponding to the work provided by the forces of gravity and radiation. The gas pressure is related to the gas energy via the ideal gas law:

$$e = \frac{p}{\gamma - 1} + \frac{\rho v^2}{2}, \tag{2.5}$$

where $\gamma$ is the adiabatic index. $\mathbf{F}$ and $P$ are related to $E$ via the flux limited diffusion (FLD) closure relation and the Eddington tensor:

$$\mathbf{F} = D\nabla E \tag{2.6}$$

$$P = fE, \tag{2.7}$$

https://doi.org/10.1017/S1743921322000230 Published online by Cambridge University Press

where the diffusion coefficient $D$ and Eddington tensor $f$ are given by an analytic recipe (see, e.g., Moens et al. 2021, Turner & Stone 2001, Levermore & Pomraning 1981).

### 2.2. *Hybrid opacity formulation*

Opacities in RHD calculations are often obtained via tables such as those provided by the OPAL project (Iglesias & Rogers 1991). These tables provide the Rosseland mean opacity calculated in the static limit as a function of gas density and temperature. However, in the case of WR outflows, such a tabulation assuming a static medium is not correctly describing the interaction between gas and radiation. Indeed, in supersonic media with high velocity gradients, the Doppler shifting of absorption lines significantly increases the total available radiation absorption capacity of the outflowing gas, rendering a more efficient stellar wind.

The winds of WR stars are driven by a combination of the Rosseland mean opacity in the static limit $\kappa^{\rm Ross}$ and a Doppler shift enhanced line opacity $\kappa^{\rm line}$. In our model we have integrated the sum of both in a hybrid opacity model (Poniatowski et al. 2021):

$$\kappa = \kappa^{\rm Ross} + \kappa^{\rm line}. \tag{2.8}$$

The Rosseland mean opacity values $\kappa^{\rm Ross}$ are tabulated by the OPAL project as function of gas density and temperature (Iglesias & Rogers 1991), while for the line opacity $\kappa^{\rm line}$ we rely on calculating the line force in the Sobolev approximation (Sobolev 1960) for a list of lines provided by Pauldrach et al. (1998). This force is then fitted to an analytic formula (Eq. (2.9)) for a range of densities, temperatures and Sobolev optical depths $t$. The best fitting line force parameters $\alpha$, $\bar{Q}$ and $Q_0$ are then tabulated as a function of density and temperature (For a general description of our line force, see Poniatowski et al. 2022, submitted). The line opacity can then be written as:

$$\kappa^{\rm line} = \kappa_0 \frac{\bar{Q}}{1-\alpha} \frac{\left((1+Q_0 t)^{1-\alpha} - 1\right)}{Q_0 t}, \tag{2.9}$$

for Sobolev optical depth:

$$t = c\kappa_0 \rho \left| \frac{dv}{dr} \right|^{-1}. \tag{2.10}$$

## 3. Results

### 3.1. *General properties of the model*

In Fig. 1 we show the model predictions for a WR star with a mass of $M_* = 10\,M_\odot$, a core radius of $R_{\rm core} = 1\,R_\odot$ and a Luminosity $L_*$ of 0.4 times the classical† Eddington Luminosity $L_{\rm Edd} = 4\pi G M_* c/\kappa_e$. The composition of the gas is hydrogen abundance $X = 0$, helium abundance $Y = 0.98$ and metalicity $Z = 0.02$, where the ratios of different metal abundances is equal to that in the Sun as described by Asplund et al. (2009). The upper and lower panels in Fig. 1 show the relative density and radial velocity of the gas in one of our 2D models. The relative density is computed by dividing the actual density by its time and lateral average. The two panels on the left show the initial conditions, and each consecutive panel to the right is at one dynamical timescale later, where $\tau_{\rm dyn} \coloneqq R_{\rm core}/1000\,{\rm km\,s^{-1}}$. Close to the stellar core, the opacity is dominated by the static Rosseland mean opacity, which is significantly high in these temperature and density regimes due to the recombination of iron. This effect is often called the iron opacity peak. In the early panels of Fig. 1, one can see that the wind is launched from these bottom regions around the iron opacity peak as the radiation force exceeds the

† Here, $\kappa_e$ is the electron scattering opacity, assumed to have a value of $0.2\,{\rm g^{-1}\,cm^2}$ in the hydrogen free atmosphere of a WR star.

https://doi.org/10.1017/S1743921322000230 Published online by Cambridge University Press

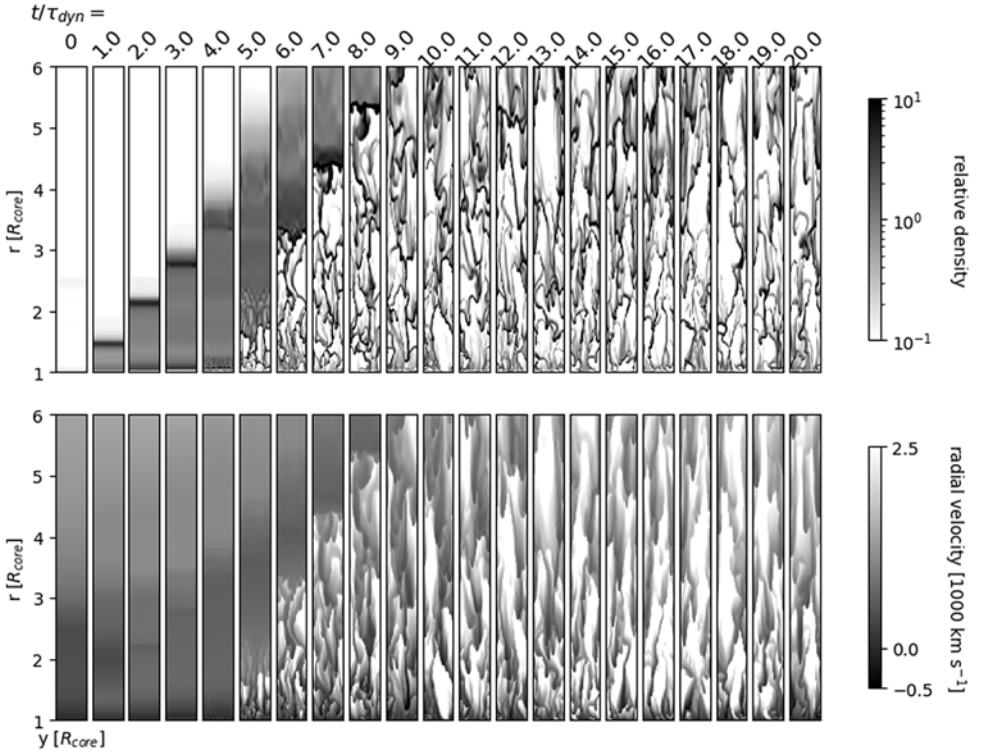


**Figure 1.** A timeseries, from left to right, displaying the relative density (top) and the radial velocity (bottom) of one of our 2D RHD WR models with a mass of $M_* = 10\,M_\odot$, a core radius of $R_{\rm core} = 1\,R_\odot$ and $L_* = 0.4 L_{\rm Edd}$. The figure shows the breakup from initial conditions and the formation of structure in the regions close to the core which are then carried outward.

force of gravity, and material starts accelerating outwards. Additionally, one can see that material starts breaking up and structure begins to form. This break-up of material is due to a convective like radiative instabillity, which has been described by Castor (2004). Linear perturbation analysis shows that when the stellar atmosphere approaches the Eddington limit and the opacity is a function of density and temperature, it can produce an absolute instability. Due to the structure formation in the low atmosphere, not all gas is able to make it out of the gravitational potential well. Indeed, gas that has been clumped together is driven less efficiently due to self-shadowing and can stagnate or even start accelerating downward back onto the stellar core. This can be seen in the bottom panels of Fig. 1, where in the bottom regions some clumps have low or negative velocities. Gas that does manage to escape will cool down which has a negative impact on the Rosseland mean opacity. However, gas in the outer wind also has a lower density, and this is where line driving takes over. Line driving is very efficient in low density environments where the continuum is optically thin. Indeed, in the optically thin limit, Eq. (2.9) approaches $\kappa^{\rm line} \propto 1/\rho^{\alpha}$. Further out in the wind, analysis shows that low density material gets accelerated by line acceleration and transfers part of its momentum to the earlier formed clumps via ram pressure thereby driving out the remaining gas in the wind. For a more in depth discussion of the general driving mechanism in our models, we refer to Moens et al. 2022, in prep.

https://doi.org/10.1017/S1743921322000230 Published online by Cambridge University Press

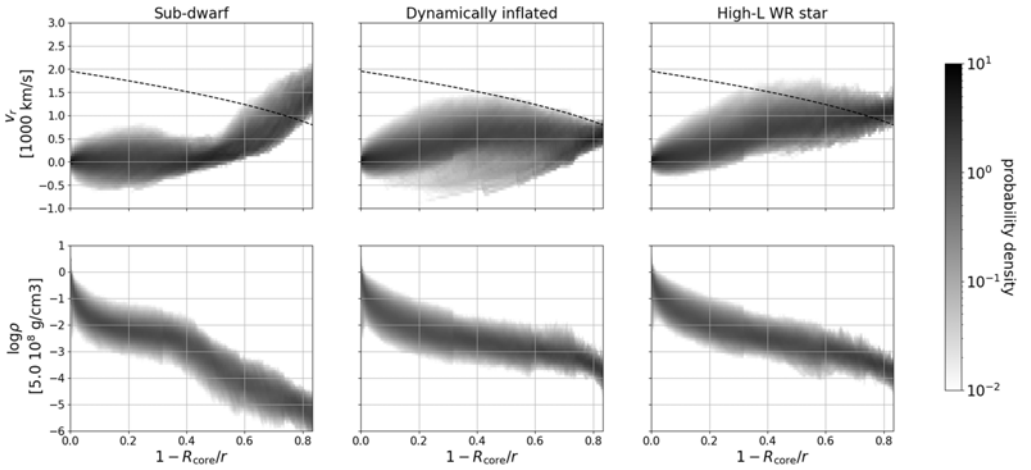


**Figure 2.** Probability density clouds of radial velocity $v_r$ (top) and gas density $\rho$ (bottom) for three 3D WR wind models with from left to right an increasing Eddington ratio: $L_*/L_{\rm Edd} = 0.33$ for the sub-dwarf, $L_*/L_{\rm Edd} = 0.46$ for the dynamically inflated WR model, and $L_*/L_{\rm Edd} = 0.67$ for the high-L WR star.

### 3.2. *Transition from sub-dwarf to WR wind*

In addition to the 2D model discussed above, here we discuss a series of three 3D models with the same stellar mass, core radius and gas composition as in the 2D model, but with three different Eddington ratios $L_*/L_{\rm Edd}$. In Fig. 2, we show density probability clouds for radial velocity (top panels) and mass density (bottom panels) for three models increasing in Eddington ratio from left to right. The probability clouds displayed in each panel are constructed by at each radius, calculating the probability density function of the gas densities and velocities present in all the lateral points from 10 3D snapshots. Histograms of these probability density functions are then displayed at each scaled radius in grey scale. The middle column of Fig. 2 corresponds to a star with an Eddington luminosity $L_*/L_{\rm Edd} = 0.46$. The velocity probability distribution of this model correspond to the non-monotonic radial velocity profiles of the dynamically inflated winds such as described by Poniatowski et al. (2021). The wind is initially accelerated due to the iron opacity peak in the Rosseland mean opacity, but afterwards fails and decelerates until line driving takes over at higher radii. One can see a large dispersion in the radial velocities as well as a distribution in density that spans a couple orders of magnitude at any given radial point. The model on the right corresponds to a model of a WR wind with a higher luminosity ($L_*/L_{\rm Edd} = 0.67$). Here, the wind morphology is largely similar to the dynamically inflated WR wind, but due to the high luminosity the wind does not significantly decelerate and the star is able to drive a higher mass-loss rate. Both the middle and right models in Fig. 2 result in a stellar wind that has a relatively high mass-loss rate ($1.5 \cdot 10^{-5}\,M_\odot\,{\rm yr}^{-1}$ and $3.2 \cdot 10^{-5}\,M_\odot\,{\rm yr}^{-1}$) and is optically thick. Finally, in the left model with $L_*/L_{\rm Edd} = 0.33$, the stellar luminosity does not suffice to actually launch a wind via the static Rosseland mean opacity alone. Instead, the launching of the wind gets delayed by expanding the core atmosphere without any significant net radial velocity before $1 - R_{\rm core}/r = 0.5$. Afterwards, the wind is launched and driven by the line driving mechanism. This model corresponds to a hot sub-dwarf, where the expanded atmosphere described here corresponds to sub-surface radiation driven convection. The actual wind is optically thin with a low mass-loss rate ($1.5 \cdot 10^{-6}\,M_\odot\,{\rm yr}^{-1}$).

https://doi.org/10.1017/S1743921322000230 Published online by Cambridge University Press

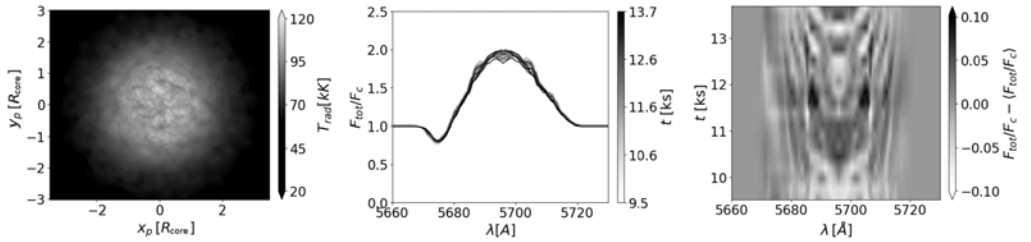


**Figure 3.** Synthetic observables for the high-L WR model. Left panel: Continuum intensity map at wavelength $\lambda = 5696\,\mathring{A}$, expressed in radiation temperature (using $I_\nu =: B_\nu\,(T_{\rm rad})$). Middle panel: Normalized flux profiles at various time snapshots of a generic line transition with central wavelength set to the CIII $\lambda$5696 line. Right panel: Mean-subtracted dynamical profile, showing the line profile variation with time. In the labels $F_c$ and $F_{\rm tot}$ are the fluxes due to continuum absorption/emission and total (continuum + line) absorption/emission.

### 3.3. *Line profile variability*

Finally, we discuss some observable aspects of our work. By converting our 3D box-in-a-wind simulations to full spherical models via a cubed sphere projection we can use a long characteristics radiation transfer solver (Hennicker et al. 2021) to calculate synthetic spectral emission lines for each time snapshot in our 3D models. Due to the structure formation of gas in the wind models, observed spectra show small scale emission and absorption features on top of the main emission line. Temporal evolution shows line profile variation (LPV). LPV's have been observed in WR stars and have been described by e.g. Lépine & Moffat (1999). The left panel in Fig. 3 shows an intensity map of the high-L WR model in the continuum. The two panels on the right show the synthetic emission lines for different snapshots and the relative variation of the emission line as a function of time.

## References

Moens, N., Sundqvist, J. O., El Mellah, I., et al. 2022, *A&A*, 657, A81
Moens, N., Poniatowski, L. G., Hennicker, L., Sundqvist, J. O., et. al. 2022, in prep.
Turner, N. J. & Stone, J. M. 2001, *ApJs*, 135, 95.
Levermore, C. D. & Pomraning, G. C. 1981, *ApJ*, 248, 321.
Poniatowski, L. G., Sundqvist, J. O., Kee, N. D., et al. 2021, *A&A*, 647, A151.
Iglesias, C. A. & Rogers, F. J. 1991, Presented at the International Workshop on Radiative Properties of Hot Dense Matter, 22
Poniatowski, L. G., Kee, N. D., Sundqvist, J. O., et al. 2022, submitted to *A&A*
Pauldrach, A. W. A., Lennon, M., et al. 1998, Properties of Hot Luminous Stars, 131, 258
Sundqvist, J. O., Owocki, S. P., & Puls, J. 2018, *A&A*, 611, A17.
Castor, J. I. 2004, Radiation Hydrodynamics, by John I. Castor, pp. 368. ISBN 0521833094. Cambridge, UK: Cambridge University Press, November 2004., 368
Asplund, M., Grevesse, N., Sauval, A. J., et al. 2009, *araa*, 47, 481.
Hennicker, L., Puls, J., Kee, N. D., et al. 2018, *A&A*, 616, A140.
Hennicker, L., Kee, N. D., Shenar, T., et al. 2021, *A&A*, accepted, *arXiv:2111.15345*
Lépine, S. & Moffat, A. F. J. 1999, *ApJ*, 514, 909.
Sobolev, V. V. 1960, Cambridge: Harvard University Press, 1960
Crowther, P. A. 2007, *araa*, 45, 177.
Hamann, W.-R., Gräfener, G., Liermann, A., et al. 2019, *A&A*, 625, A57.
Nugis, T. & Lamers, H. J. G. L. M. 2000, *A&A*, 360, 227

https://doi.org/10.1017/S1743921322000230 Published online by Cambridge University Press